Strain-engineered S-$HfSe_2$ monolayer as a promising gas sensor for detecting NH_3 A first-principles study

Yang, Huiru; Li, Junfeng; Shao, Ziyuan; Tan, Chunjian; Gao, Chenshan; Cui, Hongyuan; Tang, Xiaosheng; Liu, Yufei; Zhang, Guoqi; Ye, Huaiyu

DOI
10.1016/j.surfin.2022.102317

Publication date
2022

Document Version
Final published version

Published in
Surfaces and Interfaces

Surfaces and Interfaces 34 (2022) 102317

Contents lists available at ScienceDirect

Surfaces and Interfaces

journal homepage: www.sciencedirect.com/journal/surfaces-and-interfaces

Strain-engineered S-$HfSe_2$ monolayer as a promising gas sensor for detecting NH_3: A first-principles study

Huiru Yang [a,b], Junfeng Li [b], Ziyuan Shao [b], Chunjian Tan [c], Chenshan Gao [b], Hongyuan Cui [d], Xiaosheng Tang [e], Yufei Liu [d], Huaiyu Ye [b,d,*], Guoqi Zhang [f]

[a] Harbin Institute of Technology, Harbin 150001, China
[b] School of Microelectronics, Southern University of Science and Technology, Shenzhen 518055, China
[c] Electronic Components, Technology and Materials, Delft University of Technology, Delft 2628 CD, the Netherlands
[d] College of Optoelectronic Engineering, Chongqing University, Chongqing 400044, China
[e] College of Optoelectronic Engineering, Chongqing University of Posts and Telecommunications, Chongqing 400065, China
[f] Department of Microelectronics, Faculty of Electrical Engineering, Mathematics and Computer Science, Delft University of Technology, Delft 2628 CD, the Netherlands

ARTICLE INFO

Keywords:
Adsorption
Doped $HfSe_2$
NH_3
Strain engineering
First-principles

ABSTRACT

The development of high-performance gas sensing materials is one of the development trends of new gas sensor technology. In this work, in order to predict the gas-sensitive characteristics of $HfSe_2$ and its potential as a gas-sensitive material, the interactions of nonmetallic element (O, S, Te) doped $HfSe_2$ monolayer and small molecules (NH_3 and O_3) have been studied by first-principles based on density functional theory. The results show that the adsorption of NH_3 and O_3 on pristine $HfSe_2$ monolayer is weak, and the adsorption strength can be significantly improved by doping O. And O-$HfSe_2$ is chemical adsorption to O_3 with large adsorption energy and transfer charge, and the band gap of O—$HfSe_2$ disappears after adsorbing O_3, indicating that the adsorption of O_3 has a significant effect on the electrical properties of the substrate. These mean that O_3 is difficult to recover from the substrate surface, thus preventing O-$HfSe_2$ from developing into a sensitive material for O_3 detection. After doping S, the charge transfers and adsorption strength to NH_3 are the largest, but it is still small. So, the strain effect on the S-$HfSe_2$/NH_3 adsorption system is also studied. The results indicate that the adsorption strength of S-$HfSe_2$ to NH_3 can be enhanced by stretching S-$HfSe_2$ along x-axis. After absorbing NH_3, the conductivity of x-axis strained S-$HfSe_2$ changes, which suggest its sensitivity. And the predicted recovery times of S-$HfSe_2$ surfaces with ε_x=4%, 6% and 8% are 0.027 s, 1.153 s and 102.467 s, respectively, which suggests that the S-$HfSe_2$ monolayer has the potential to be developed as a sensitive material for NH_3 detection. These adsorption mechanism studies can also serve as a theoretical foundation for the experimental design of gas-sensing materials.

1. Introduction

Gas sensors can detect gas concentration and composition, which is critical in environmental protection and safety monitoring. Gas sensors are now widely used to detect toxic, hazardous, explosive, and volatile substances, as well as to monitor the greenhouse effect and air pollution [1–3]. In the face of more and more special signals and special environments, the development of high-performance gas sensing materials is one of the development trends of new gas sensor technology. Due to their excellent mechanical, electrical, and optical properties, such as ultra-high carrier mobility, tunable band structure and gas sensing properties, two-dimensional (2D) materials have attracted the attentions of researchers in the field of gas-sensitive materials [4–6]. In particular, two-dimensional transition metals disulfides (TMDs; MX_2: M = Mo, W; X = S, Se) are promising gas sensing materials that attracts attention due to their large specific surface area, excellent electrical properties, and active surface [7,8]. Perhaps the most attractive feature of TMDs-based gas sensors is their ability to detect gas molecules at room temperature (RT), which stems from the unique electronic properties presented by the two-dimensional atomic structure. Based on this unique feature, the TMDs can be used as low-power gas sensors.

To date, TMDs materials such as MoS_2 [9,10], $MoSe_2$ [11,12], WS_2

* Corresponding author at: School of Microelectronics, Southern University of Science and Technology, Shenzhen 518055, China.
E-mail address: h.ye@tudelft.nl (H. Ye).

https://doi.org/10.1016/j.surfin.2022.102317
Received 7 June 2022; Received in revised form 11 August 2022; Accepted 27 August 2022
Available online 7 September 2022

[13,14], WSe_2 [15] have been extensively studied for gas sensing. Guo et al. [12] fabricated a high-performance epidermal gas detector based on $MoSe_2$ nanosheets that can monitor NO_2 and NH_3 at room temperature and respond quickly. Kumar et al. [10] review and discuss the results of MoS_2-based gas sensors, indicating that 2D MoS_2 could be a promising material for developing high-performance room-temperature gas sensors. Modifying the surface of TMDs is also desirable in order to improve and optimize device performance. Surface modification techniques include the use of dopants to replace or bond to specific atoms in the substrate material. Baek et al. [16] functionalized the MoS_2 surface with Pd, fabricating a sensor with high sensitivity to hydrogen. Through the sulfurization of WSe_2, Kim's team [17] created a large-area uniform $WS_{2x}Se_{2-2x}$ alloy, and the results indicated that the large-area $WS_{2x}Se_{2-2x}$ alloy's gas sensing capability was significantly improved.

While other kinds of TMDs are less studied, such as HfX_2 and ZrX_2 (X = S, Se and Te). $HfSe_2$ monolayer with high carrier mobility and small band gap has been predicted theoretically [18,19], and the monolayer has been successfully prepared through experiments [20,21], which indicates that it has the potential to be used as a gas sensing material. Cui Hao et al. [22,23] have studied the adsorption behavior of intrinsic, Pd-doped and Pt-doped $HfSe_2$ monolayer to some toxic gases (SOF_2, SO_2, NO_2) by first-principles. However, there is a lack of research on other small molecules. Ammonia (NH_3) is a very important raw material in many fields such as industry, agriculture, food processing, medicine [24,25]. But NH_3 is also a harmful gas that can cause serious harm to the body even in low concentrations by injuring the skin, eyes, throat, or lungs [26,27]. Ozone (O_3) also belongs to this type of gas, which has a very important impact on people's lives. Besides being used for water purification and disinfection, O_3 is also widely used for disinfection in the food and pharmaceutical industries [28,29]. However, excess ozone can have many adverse effects on human health, ecosystems and agricultural production [30,31]. Therefore, in the field of production and life, the monitoring of O_3 and NH_3 content is particularly important.

Herein, for the first time, we construct adsorption models of NH_3 and O_3 adsorption on pristine and X-doped (X=O, S, and Te) $HfSe_2$ monolayer surface, and calculate the adsorption behaviors to explore their potential as NH_3 and O_3 gas sensors. The adsorption strength of the X-$HfSe_2$/gases system is higher than that of pristine $HfSe_2$, with O-$HfSe_2$ having the highest adsorption strength. The results show that O_3 is chemisorbed on the surface of O-$HfSe_2$ with larger adsorption energy and charge transfer. The electrical property of O-$HfSe_2$ also change with the disappearance of the band gap after adsorbing O_3. Besides, the interaction of S-$HfSe_2$ with gas molecules is physical adsorption, and the adsorption energy is small. The adsorption of NH_3 by S-$HfSe_2$ can be enhanced by applying tensile strain, and the fast recovery is maintained. Therefore, S-$HfSe_2$ has potential applications as a sensitive material for NH_3 detection. This research offers theoretical guidance for the manufacturing of $HfSe_2$-based gas sensors as well as new insights into the design of atomic-scale high-sensitivity gas sensors.

2. Method

The code DMOL^3 is used to calculate all structural relaxation and electrical characteristics in this work [32]. To approximate the exchange correlation energy, generalized gradient approximation (GGA) of the Perdew-Burke-Ernzerhof (PBE) function type is used in this work [33,34]. This may make the calculation more precise due to the uneven distribution of electrons being taken into account [34]. The Tkatchenko and Scheffler's (TS) method was applied to depict the long-range effects and the weak intermolecular forces in the dispersion corrections (DFT-D) parameters [35]. The substrate (X-$HfSe_2$) contains transition metals, so it is processed with DFT Semi-core pseudopotential (DSPP) [36,37]. In the basis set, the Double-ζ basis plus polarization (DNP) numerical atomic orbital is used [38]. The orbit cutoff radius is set to 5.3 Å, the test results are shown in Table. S1 of Supplementary Material. The convergence conditions for the structural relaxation are as follows, total energy and maximum displacement convergence requirements are 10^{-5} Ha (1 Ha = 27.21 eV) and 0.005 Å, respectively [22,23]. Also, until the maximum residual force is less than 0.002 Ha/Å, the geometry is relaxed. In the Z direction, a space layer of 25 Å is utilized to reduce interactions between adjacent layers. For the k-point mesh generation, we calculate the total energy and average atomic energy of $HfSe_2$ cell with different k-point values, as shown in Fig. S1 of Supplementary Material. The result indicates $3 \times 3 \times 1$ for $HfSe_2$ supercell can meet the convergence condition. So, the $5 \times 5 \times 1$ and $9 \times 9 \times 1$ Monkhorst-Pack grid are used for structural relaxation and electrical properties, respectively.

The formula (1) is used to calculate the adsorption energy (E_a) of the gas with the X-$HfSe_2$ monolayer:

$$E_a = E_{(Sub+gas)} - E_{(Sub)} - E_{(gas)} \tag{1}$$

where $E_{(Sub\ +\ gas)}$, $E_{(Sub)}$ and $E_{(gas)}$ are the total energy of substrate/gases adsorption system, isolated substrate and the separated gases molecules, respectively. Positive value means the adsorption cannot proceed spontaneously, while negative value means the adsorption can occur spontaneously. And the smaller the E_a, the stronger the adsorption of gas molecules on the $HfSe_2$ monolayer.

In order to completely analyze the charge transfer between the gas and X-$HfSe_2$ monolayer, Mulliken charge [39] analysis was conducted in this work. The charge difference for the gas *i* after and before adsorption, was calculated using the following equation:

$$\Delta Q_i = Q_{i(in\ system)} - Q_{i(i\ vacuum)} \tag{2}$$

where Q_i is the value of Mulliken charge of the *i*. Subscript "*i*" denotes the gas molecule. The charge difference, ΔQ, is a measure of the extent of charge shifted to, or, from the gas molecule. The positive ΔQ means that the gas is electron donors, while negative ΔQ means gas is electron acceptors.

The following formula (3) is used to compute the charge density difference (CDD):

$$\Delta\rho = \rho_{(Sub+gas)} - \rho_{(Sub)} - \rho_{(gas)} \tag{3}$$

where $\rho_{(Sub\ +\ gas)}$, $\rho_{(Sub)}$ and $\rho_{(gas)}$ are the charge densities of the whole adsorption system, separated substrate and gas molecule, respectively.

The unit cell of $HfSe_2$ monolayer is relaxed firstly, with the optimized lattice constant of 3.77 Å, which is consistent with the values (3.76 Å) in the literature [40]. And then using the optimized unit cell, the 3×3 supercell of $HfSe_2$ monolayer is generated. The X-doped $HfSe_2$ (X-$HfSe_2$, X = O, S, Te) monolayer is constructed by replacing one Se atom on the

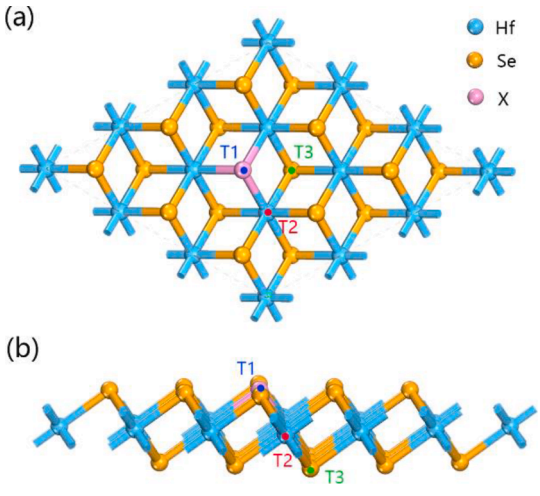

Fig. 1. The structure of pristine and doped $HfSe_2$ (X-$HfSe_2$, X = O, S, Te) monolayer and its adsorption sites. (a) top view, (b) side view.

upper surface with an X atom, as shown in Fig. 1. And the optimized structure of X-$HfSe_2$ monolayer is shown in Fig. S2. In addition, the AIMD simulations were set by 5000 fs with the temperature of 300 K to check the stability for all X-$HfSe_2$ structures, as displayed in Fig. S3.

To study the adsorption properties between the X-$HfSe_2$ monolayer and the gases (NH_3 and O_3), the initial model needs to be established considering the adsorption sites of the substrate and the placement of the gases. We considered three possible adsorption sites for X-$HfSe_2$, including on the top of Se/X (T1 site), Hf (T2 site), and Se-down (T3 site), as shown in Fig. 1. And the gas can be placed parallel or vertical to the different adsorption sites of X-$HfSe_2$, so six configurations are considered for each gas molecule. The initial adsorption distance is set as 3 Å. All of these initial adsorption models are relaxed using the same method. First, the optimal adsorption configuration and adsorption property of pristine $HfSe_2$ interacting with gas are calculated as a comparison to study the adsorption properties of doped $HfSe_2$. Then, the adsorption properties of doped $HfSe_2$ are investigated.

3. Result and discussion

3.1. The adsorption of pristine and X-$HfSe_2$

To investigate the adsorption properties of pristine and X-doped $HfSe_2$ (X-$HfSe_2$, X=O, S, Te) for NH_3 and O_3, an adsorption model is built using the method described above, and the best adsorption configuration, adsorption energy, and charge transfer are estimated. Fig. 2 shows the best adsorption configurations of pristine and X-$HfSe_2$ for NH_3 and O_3 with the minimum energy.

The optimized pristine $HfSe_2$ adsorption systems are shown in Fig. 2 (a)-(b). When adsorption of NH_3, H atom tends to be close to Se atoms with the large adsorption distance (3.258 Å). When O_3 is adsorbed, O1 atom (O atoms on the edge of O_3) get close to Se atom on the surface of $HfSe_2$ and the adsorption distance (3.114 Å) is also large. And the structure of both the substrate and the gas molecules hardly changed. In the adsorption of Te-$HfSe_2$, a similar result can be seen, as shown in Fig. 2(g)-(h). Fig. 2(c)-(d) shows the optimized O-$HfSe_2$/gas adsorption system. Remarkably, NH_3 and O_3 are closer to the surface of O-$HfSe_2$ monolayer than pristine $HfSe_2$. Both the N atom of NH_3 and the O1 (O atom at the edge of O_3) atom of O_3 are close to the Hf atom of the O-$HfSe_2$ monolayer, resulting in shorter adsorption distances of 2.402 Å and 1.992 Å, respectively. The O-Hf bond length measured in the experiment is larger than 2 Å [41], while the adsorption distance is less than this value, which suggests that a chemical bond could form between the O and Hf atom, and there should be chemisorption between O_3 and O-$HfSe_2$. And after adsorption of O_3, the structures of O-$HfSe_2$ and O_3 changed significantly, as shown in Fig. 2(d). Both O1-O2 bond and O-Hf bond are elongated from 1.279 Å and 2.134 Å to 1.736 Å and 2.173 Å, and the angle of O-Hf-Se increases from 103.851° to 120.862° (Fig. S4(d)), which can be explained by the significant contact between the O and Hf atom. In the adsorption of NH_3, a similar condition can be observed, where the angle of O-Hf-Se is also increased from 103.851° to 120.387°, as shown in Fig. S4(c), causing the N atom to more easily approach the Hf atom, thereby increasing their interaction. In S-$HfSe_2$/NH_3 adsorption system, as shown in Fig. 2(e), N atom of NH_3 is also close to Hf atom with shorter adsorption distance (2.515 Å), which is similar to O-$HfSe_2$ but no obvious deformation. While adsorption of O_3, as shown in Fig. 2(f), the adsorption configuration is similar to the pristine $HfSe_2$ and adsorption distance is also large (3.172 Å).

When compared to the other doped monolayers considered in this study, the adsorption between O-$HfSe_2$ and gases is the greatest. The

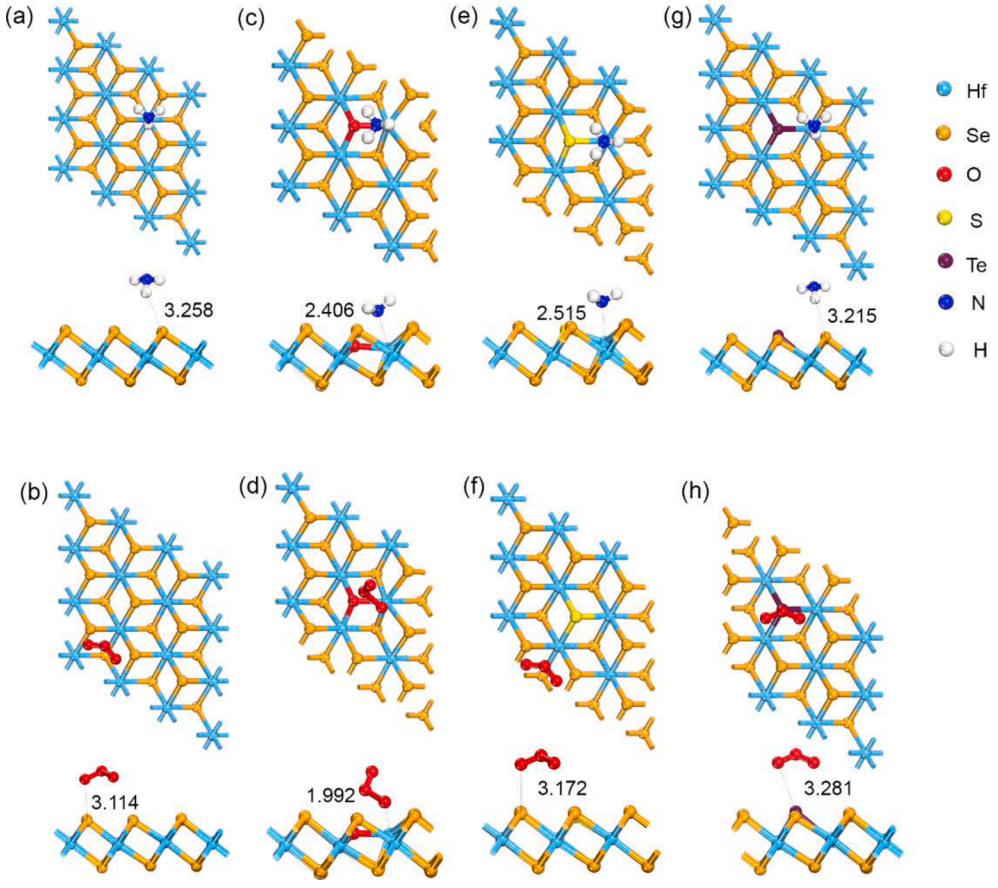

Fig. 2. The optimal adsorption configuration of (a) pristine $HfSe_2$/NH_3, (b) pristine $HfSe_2$/O_3, (c) O-$HfSe_2$/NH_3, (d) O-$HfSe_2$/O_3, (e) S-$HfSe_2$/NH_3, (f) S-$HfSe_2$/O_3, (g) Te-$HfSe_2$/NH_3 and (h) Te-$HfSe_2$/O_3. The adsorption distance is marked in the figure (unit: Å).

electronegativity, bond length and bond angle of the substrate and gases are utilized to explain why O-$HfSe_2$ is more active. The substrate atoms (X-$HfSe_2$) include Hf, Se, O, S, and Te, with electronegativities of 1.31, 2.55, 3.44, 2.58, and 2.10, respectively, with the Hf atom being the least electronegative. And the electronegativities of N and H in NH_3 are 3.04 and 2.20, respectively. Therefore, it is easier for N and Hf to approach and interact theoretically. However, in pristine $HfSe_2$, due to its sandwich structure, Hf atom is in the middle layer, and the bond angle of Se-Hf-Se is small (89.058°), which prevents them from approaching each other, so only H atom interact with the surface Se. After doping with O, the bond angle of O-Hf-Se increases to 103.851°, which reduces the obstacle of N approaching Hf. Therefore, the N of NH_3 interacts strongly with Hf, which finally reduces the adsorption distance and enhance their interaction so that the adsorption configuration deforms significantly. Similarly, the electronegativity of O in O_3 are 3.44, which makes it easier to approach and interact with Hf in theory. Thus, the adsorption of O_3 is also enhanced by doping O.

The adsorption energy (E_a) is calculated to study the adsorption strength between the X-$HfSe_2$ monolayer and gas, as shown in Table 1. The smaller the value, the stronger the adsorption of the gas to the substrate. For the adsorption of NH_3 and O_3 by pristine $HfSe_2$, the adsorption energies are −0.340 eV and −0.416 eV, respectively, indicating that the interactions between gases and the substrate are weak. After doping with O, the absolute value of the adsorption energy increases significantly, which are −1.138 eV and −1.183 eV, respectively, indicating that the adsorption strength of the gas on the substrate surface is improved. For the S-$HfSe_2$/gases and Te-$HfSe_2$/gases adsorption systems, the adsorption energy only changed slightly. After doping with S and Te, the adsorption energy for NH_3 (O_3) decreases from −0.340 eV (−0.416 eV) to −0.466 eV (−0.425 eV) and −0.444 eV (−0.446 eV), which means that the increase in adsorption strength is not obvious.

As a result, the interaction strengths of different substrates with NH_3 are as follows: O-$HfSe_2$ > S-$HfSe_2$ > Te-$HfSe_2$ > $HfSe_2$. The order of adsorption strength for O_3 by X-$HfSe_2$ monolayer is O-$HfSe_2$ > Te-$HfSe_2$ > S-$HfSe_2$ > $HfSe_2$. When compared to pristine $HfSe_2$, the adsorption strength of O-$HfSe_2$ for NH_3 and O_3 is clearly enhanced, while the other two doping systems have little effect.

As one of the important parameters for studying the adsorption strength between the X-$HfSe_2$ monolayer and gas, charge transfer has been studied further by calculating Mulliken charge [42]. The results also show in Table 1. In the pristine $HfSe_2$/gases system, charge transfer of NH_3 and O_3 are 0.056 e and −0.157 e, respectively, which indicates that they are electron donors and acceptors, respectively. For the adsorption of NH_3, the charge transfer increases to 0.268 e and 0.270 e after doping with O and S, while it decreases to 0.033 e after doping Te. When adsorbing O_3, the charge transfer also increases to −0.417 e after doping with O, while after doping S and Te, the change is small. Detailed charge analysis is specifically analyzed in the Fig. S5 of Supplementary Material. The charge transfer of the O-$HfSe_2$/gas and S-$HfSe_2$/NH_3 system is significant, indicating the strong interaction between them, which is consistent with the previous calculations of adsorption energies and optimal adsorption configurations.

In the following section, the electrical properties of the X-$HfSe_2$/gas adsorption systems are calculated in order to fully study and understand the mechanism.

Table 1
The adsorption energy (E_a) and charge transfer (ΔQ) of pristine $HfSe_2$ and X-$HfSe_2$ for NH_3 and O_3.

	E_a(eV)		ΔQ (e)	
	NH_3	O_3	NH_3	O_3
Pristine $HfSe_2$	−0.340	−0.416	0.056	−0.157
O-$HfSe_2$	−1.138	−1.183	0.268	−0.417
S-$HfSe_2$	−0.466	−0.425	0.270	−0.154
Te-$HfSe_2$	−0.444	−0.446	0.033	−0.179

3.2. Electrical properties of X-$HfSe_2$ adsorption system

The gas interaction with X-$HfSe_2$ can be understood by the charge density difference (CDD), which helps to predict the charge redistribution behavior between the substrate and gas, and can get a deeper insight into the interaction mechanism between gas molecule and substrate.

CDD: The calculated CDD results are shown in Fig. 3, with the two isosurfaces in light green (0.02 e/Å^3) and pink (−0.02 e/Å^3), respectively. Electron density accumulates and dissipates in light green and pink areas, respectively. In all the adsorption systems depicted in Fig. 3, significant charge accumulation and dissipation occurred between the O_3 and O-$HfSe_2$ monolayer, as shown in Fig. 3(b), which further illustrates the strong interaction between them. The charge accumulation in the shared region represents the formation of important chemical bonds, which indicates the formation of chemisorption between the O_3 and O-$HfSe_2$ monolayer. It is consistent with the results of adsorption performance. While there is little charge redistribution between Te-$HfSe_2$, S-$HfSe_2$ and O_3, as shown in Fig. 3(d) and (f), which is much smaller than that of O-$HfSe_2$/O_3 system. As for NH_3, as shown in Fig. 3(a) and (c), there is a relatively large charge accumulation and dissipation. The charge is dissipated near H atom of NH_3 and Hf atom of substrate, and accumulated near N atom of NH_3. The results are in agreement with the above conclusions that NH_3 prefers to be close to Hf atom. However, there is almost no charge redistribution between Te-$HfSe_2$ and NH_3, as shown in Fig. 3(e), which is consistent with the results of the above adsorption parameters (ΔQ=0.033 e).

The electrical properties of O-$HfSe_2$: The electrical properties of O-$HfSe_2$ after gas adsorption are calculated, including band structure, density of states (DOS), and partial density of states (PDOS), which can help to better understand the adsorption mechanism and study the electrical properties of O-$HfSe_2$. The band structure can describe band distribution curve and band gap. DOS and PDOS can be used to describe how gas molecules contribute to the total electronic state of an adsorption system. Fig. 4 depicts the band structures of the O-$HfSe_2$ monolayer before and after gas adsorption. After adsorption of NH_3, the band structure of the O-$HfSe_2$/NH_3 system hardly changed, and only the conduction band (CB) shifted up slightly. Therefore, after adsorption of NH_3, the band gap of O-$HfSe_2$ increases from 0.776 eV to 0.792 eV. While some impurity states are generated near the Fermi level of the O-$HfSe_2$ monolayer after O_3 adsorption, due to the partial contribution of the p-orbital of the O atom in O_3. And the valence band (VB) region moves up. So the band gap of O-$HfSe_2$ disappears after adsorbing O_3, which means that the O-$HfSe_2$ went from a semiconductor to a metallic material. These results show that the adsorption of O_3 has a significant impact on the electrical properties of O-$HfSe_2$, further indicating that the interaction between them is strong.

And, as shown in Fig. 4(d), after absorbing NH_3, the DOS is nearly identical to that of pristine O-$HfSe_2$. The O-$HfSe_2$ monolayer contributes the majority of the DOS of the entire adsorption system, indicating that the electrical properties of O-$HfSe_2$ are not significantly changed by NH_3 adsorption. Furthermore, according to the PDOS, there is no orbital hybridization between O-$HfSe_2$ and NH_3 near the Fermi level. These findings show that NH_3 is physically adsorbed onto the surface of the O-$HfSe_2$ monolayer. However, when O_3 is adsorbed to the surface of O-$HfSe_2$, the DOS significantly changes, as shown in Fig. 4(e). The peak of DOS is shifted to the right, especially in the valence band region (energy < 0 eV). And at 1.5 eV and −1.5 eV, obvious orbital hybridization occurs between the p orbital of O (O-p) and the d orbital of Hf (Hf-d), which indicates that chemical bond is likely to be formed between them. These findings help to explain the strong reaction between O_3 and Hf atoms in the O-$HfSe_2$ monolayer, which is consistent with the above adsorption property results.

A large number of literatures [42,43] show that physical adsorption is more favorable for sensitive materials due to its fast response and good repeatability, while chemisorption is not suitable due to its difficulty in

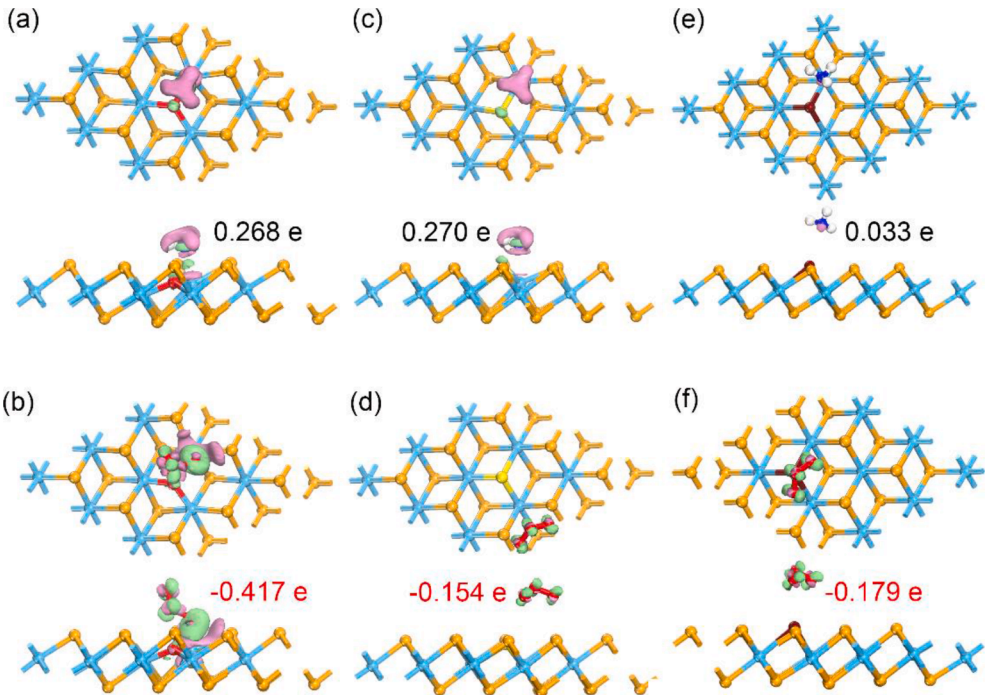

Fig. 3. CDDs of (a)O-$HfSe_2/NH_3$, (b)O-$HfSe_2/O_3$, (c)S-$HfSe_2/NH_3$, (d)S-$HfSe_2/O_3$, (e)Te-$HfSe_2/NH_3$ and (f)Te-$HfSe_2/O_3$ systems. The light green (pink) represents charge accumulation (dissipation). The isosurface value is set as 0.02 e/$Å^3$.

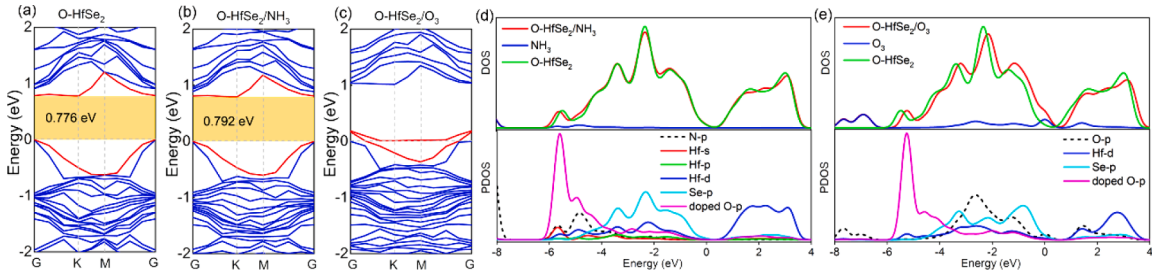

Fig. 4. The band structure of (a) O-$HfSe_2$, (b) O-$HfSe_2/NH_3$ and (c) O-$HfSe_2/O_3$. The DOS (up) and PDOS (down) of (d) O-$HfSe_2/NH_3$ and (e) O-$HfSe_2/O_3$ adsorption system. The Fermi level is at 0 eV.

recovery, which prevents the application of O-$HfSe_2$ as a O_3 sensor. The possibility of O-$HfSe_2$ as an NH_3 sensor is discussed later.

The electrical properties of S-$HfSe_2$: The electrical properties of the S-$HfSe_2$ monolayer before and after gas adsorption are shown in Fig. 5. After adsorption of NH_3, the band structure of S-$HfSe_2$ hardly changed, only CB and VB moved up and down slightly. Therefore, the band gap changes from 0.618 eV to 0.706 eV. Furthermore, Fig. 5(d) shows that the DOS of S-$HfSe_2$ after NH_3 adsorption is nearly the same as before adsorption, indicating that NH_3 is very little effect on the electrical properties of the entire system. And based on PDOS, no orbital hybridization occurs between the S-$HfSe_2$ and NH_3 near the Fermi level. These findings show that NH_3 is physically adsorbed onto the surface of the S-$HfSe_2$ monolayer.

After adsorbing O_3, new band is generated around 0.5 eV, resulting the band gap decreases from 0.618 eV to 0.432 eV. And the peak of DOS around −1.4 eV is increased, as shown in Fig. 5(e). These are all because of the contribution of O_3. The orbital hybridization weakly occurs at −1.4 eV between O-p of O_3 and Se-p, S-p of S-$HfSe_2$. And there is a new

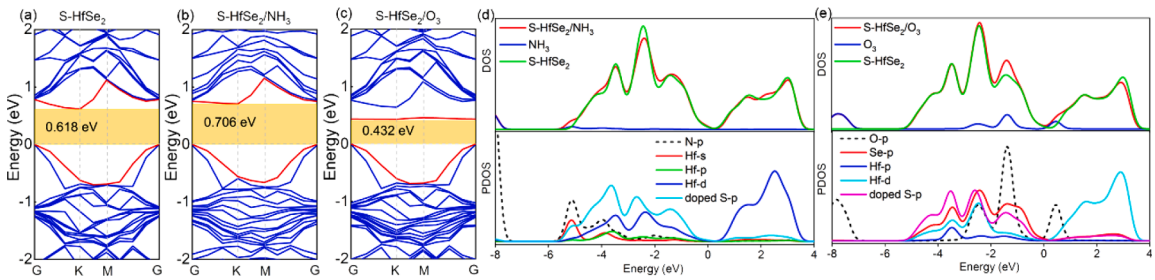

Fig. 5. The band structure of (a) S-$HfSe_2$, (b) S-$HfSe_2/NH_3$ and (c) S-$HfSe_2/O_3$. The DOS (up) and PDOS (down) of (d) S-$HfSe_2/NH_3$ and (e) S-$HfSe_2/O_3$ adsorption system. The Fermi level is at 0 eV.

peak generated near 0.5 eV. Therefore, the band gap and DOS of S-$HfSe_2$ change after adsorption of O_3. But the adsorption energy is not large, which prevents S-$HfSe_2$ from detecting O_3.

The electrical properties of Te-$HfSe_2$: Fig. 6 shows the electrical properties of Te-$HfSe_2$ monolayer after gas adsorption, which is similar to S-$HfSe_2$. After adsorption of NH_3, the band structure of Te-$HfSe_2$ hardly changed, and only the CB shifted slightly downward. Therefore, the band gap decreases from 0.500 eV to 0.442 eV. Furthermore, Fig. 6 (d) shows that the DOS of Te-$HfSe_2$/NH_3 is almost the same as before adsorption, indicating that NH_3 has little effect on the electrical properties of the whole system. And near the Fermi level, there is no orbital hybridization between Te-$HfSe_2$ and NH_3. These results suggest that NH_3 is physically adsorbed on the surface of the Te-$HfSe_2$ monolayer.

After adsorption of O_3, the band structure of Te-$HfSe_2$ shows that a new energy band is generated around 0.4 eV, which reduces the band gap from 0.500 eV to 0.392 eV. And the DOS peak around −1.4 eV increases, and a new weak peak is generated around 0.5 eV, as shown in Fig. 6(e). As can be seen from PDOS, these are all because of the O-p contribution of O_3. Weak orbital hybridization occurs at −1.4 eV and −2.5 eV between O-p of O_3 and Te-p, Hf-d of Te-$HfSe_2$. Therefore, the band gap and DOS of Te-$HfSe_2$ changes after adsorbing O_3.

The above calculation results show that O-$HfSe_2$ has a strong adsorption effect on NH_3 and O_3, with O_3 adsorption being chemical and NH_3 adsorption being physical. Both O_3 and NH_3 are physically adsorbed by S-$HfSe_2$ and Te-$HfSe_2$, but the adsorption strength is weak. And the above analysis shows that the reason for the adsorption of NH_3 onto S-$HfSe_2$ monolayer is the large charge transfer between N atom of NH_3 and Hf of S-$HfSe_2$. These imply that the adsorption strength of NH_3 can be improved by enhancing the interaction between N atom and Hf atom. When stretching S-$HfSe_2$ along the x axis, N atom and Hf atom are closer to each other and their interaction could be enhanced. Therefore, the next section calculates the effect of the x-axis strain on the S-$HfSe_2$/NH_3 adsorption system. In addition, the coverage of NH_3 on S-$HfSe_2$ surfaces have been calculated and discussed. The results have been added in Supplementary Material.

3.3. Improvement of NH_3 sensing performance by x-axis strained S-$HfSe_2$

The adsorption energy and charge transfer of S-$HfSe_2$ to NH_3 under different strains (from −4% to 8%) along the x-axis, y-axis and biaxial strain are calculated to validate that the adsorption strength of S-$HfSe_2$ for NH_3 may be improved by stretching S-$HfSe_2$.

Fig. 7 shows the trend of E_a, ΔQ and d with x-axis, y-axis and biaxial strain from −4% to 8%. Both the E_a and d of S-$HfSe_2$/NH_3 adsorption system briefly decrease at tensile strain of ε_x=0~8%, and increase at compression of ε_x=0~−4%. And the charge transfer (ΔQ, Fig. 7b) increases systematically with increasing x-axis tensile strain. The same goes for the variation trends of E_a, ΔQ and d when y-axis (red) or biaxial strain (blue) is applied. The above results indicate that the tensile strains in different directions significantly increase the adsorption strength of S-$HfSe_2$ for NH_3, thereby improving the performance of the strained S-$HfSe_2$-based NH_3 sensor. The difference is that the amount of change induced by biaxial strain is larger. However, it is more difficult to realize biaxial strain than uniaxial strain experimentally. In addition, since the structure of the substrates along the x-axis or y-axis is the same, there is no significant difference in the effect of the strain on the adsorption parameters (E_a, ΔQ and d), which is almost the same. Therefore, the following studies mainly focus on the x-axis strain effect.

And the adsorption of x-axis strained S-$HfSe_2$ to O_3 is also calculated as a comparison. For O_3, the variation trend of E_a with x-axis strain is completely different from that for NH_3, as shown in Table S1. When O_3 is adsorbed on the unstrained S-$HfSe_2$ monolayer, the E_a is −0.126 eV. As the x-axis tensile strain increases from 0% to 6%, it increases from −0.126 eV to −0.118 eV, suggesting the adsorption strength weakens with increasing strain. The ΔQ also decreases with increasing x-axis tensile strain, in the opposite direction of NH_3. As a result, x-axis strain can help to improve the selectivity of an NH_3 sensor based on S-$HfSe_2$ monolayer to some extent.

In addition, at strain of ε_x=4%, the band structure, DOS and PDOS of S-$HfSe_2$/NH_3 are calculated and described in Fig. 8. When NH_3 is adsorbed onto S-$HfSe_2$ with ε_x=4%, the band gap increased from 0.700 eV to 0.819 eV, indicating that the conductivity of the substrate changed significantly after adsorption of NH_3 compared to before adsorption. In addition, after adsorption of NH_3, the S-$HfSe_2$ monolayer with ε_x=4% is transformed from an indirect band-gap to a direct band-gap, which makes it easier for electrons to be excited from the valence band to the conduction band, so the optical properties of the substrate after adsorption of NH_3 will also change accordingly.

And according to Fig. 8(c), after adsorption of NH_3, the DOS of S-$HfSe_2$ with ε_x=4% is almost the same as before adsorption, further indicating that the DOS of the entire S-$HfSe_2$/NH_3 system is mainly contributed by the substrate. The PDOS also shows that no orbital hybridization occurs between S-$HfSe_2$ with ε_x=4% and NH_3 near the Fermi level. At approximately −5.5 eV, far from the Fermi level, apparent orbital hybridization occurs between N-p and Hf-s, p, d. These results demonstrate that NH_3 is still physically adsorbed on the S-$HfSe_2$ monolayer with ε_x=4%, just like when no strain is applied. This also further indicates that the adsorption strength of S-$HfSe_2$ for NH_3 can be enhanced by stretching S-$HfSe_2$ along the x-axis, which can provide theoretical guidance for sensitive materials design.

3.4. Sensing behavior prediction of S-$HfSe_2$ for NH_3

Aforementioned studies show that S-$HfSe_2$ is a potentially sensitive material for the detection of NH_3, and it is worth mentioning that the conductivity (σ) and recovery time (τ) are important factors for gas sensors. Therefore, this section predicts the potential of x-axis strain-engineered S-$HfSe_2$ as an NH_3 sensor by calculating conductivity and recovery time.

After NH_3 adsorption, the conductivity of the substrate changes. And its change rate determines the sensitivity of the device. The band gap value is an important factor in determining S-$HfSe_2$ conductivity. The following formula (4) expresses the relationship between the band gap and conductivity [44]:

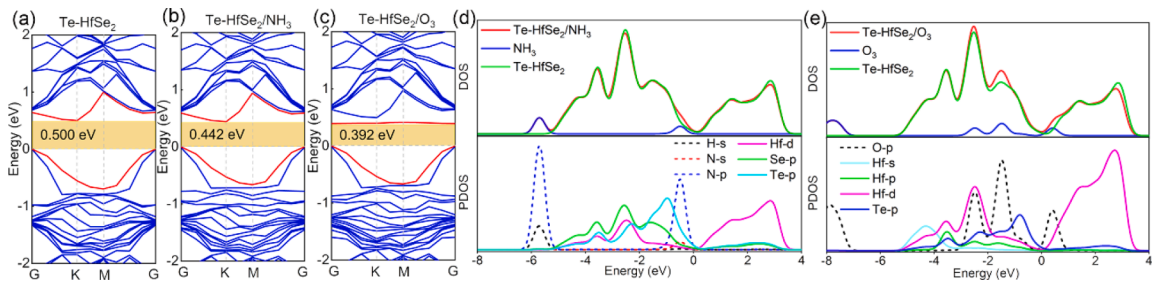

Fig. 6. The band structure of (a) Te-$HfSe_2$, (b) Te-$HfSe_2$/NH_3 and (c) Te-$HfSe_2$/O_3. The DOS (up) and PDOS (down) of (d) Te-$HfSe_2$/NH_3 and (e) Te-$HfSe_2$/O_3 adsorption system. The Fermi level is at 0 eV.

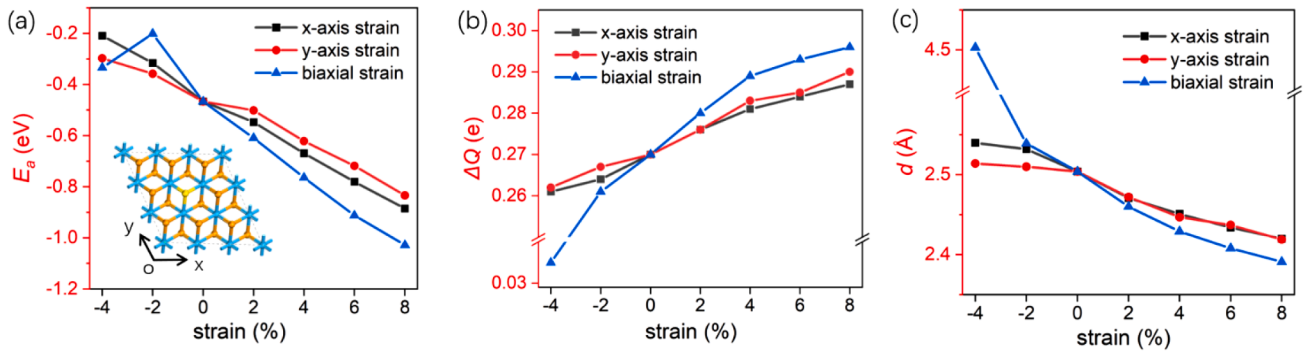

Fig. 7. The variation curves of (a) E_a, (b) ΔQ and (c) d with x-axis, y-axis and biaxial strain from −4% to 8% in S-$HfSe_2$/NH_3 adsorption system.

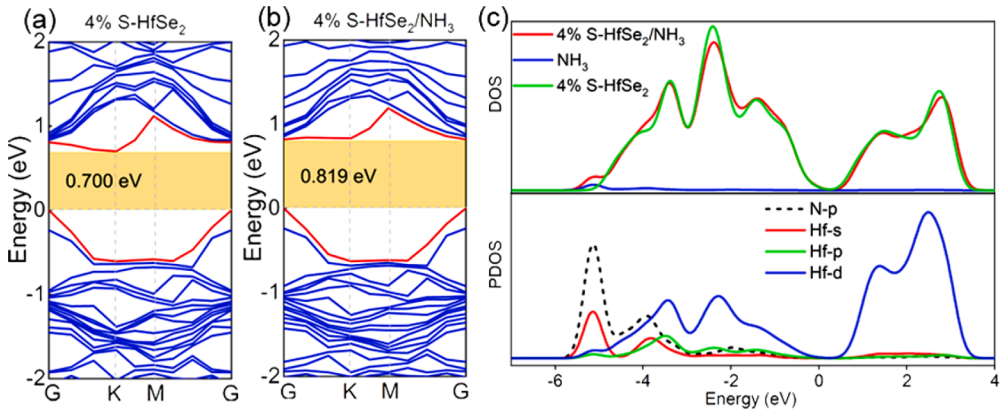

Fig. 8. The band structure for S-$HfSe_2$ with ε_x=4% (a) before and (b) after adsorbing NH_3, (c) the DOS (up) and PDOS (down) of S-$HfSe_2$/NH_3 with ε_x=4%. Fermi level is at 0 eV.

$$\sigma \propto e^{-E_g/2kT} \tag{4}$$

where k and T represent the Boltzmann constant and temperature, respectively, and E_g represents the band gap.

This formula states that the larger the band gap of the substrate material, the lower the conductivity at a given temperature T. In addition, it is also demonstrated that the greater the rate of change in the band gap, the greater the rate of change in conductivity. And sensitivity can be characterized by the change rate of conductivity, which suggests that the greater the change rate of band gap, the higher the sensitivity. After adsorption NH_3, the band gap change rates of S-$HfSe_2$ under ε_x=2%, 4%, 6%, and 8% strain are 16.3%, 17.0%, 14.2% and 11.2%, respectively, which imply that conductivity of substrate decreases after adsorbing NH_3 and the change rate of S-$HfSe_2$ with ε_x=4% is the largest. Combined with the adsorption properties and electrical properties studied above, it is suggested that x-axis strained S-$HfSe_2$ can be used as a potential sensing material for the detection of NH_3.

To further validate the reusability of the x-axis strained S-$HfSe_2$ monolayer as a gas sensor for NH_3 detection, the recovery time is calculated, which is a known parameter that determines the quality of a gas sensor. Theoretical methods for estimating recovery time are based on transition state theory, which can be calculated using formula (5) [45]:

$$\tau = w^{-1} e^{-E^*/kT} \tag{5}$$

where w, k, T, E^* are the attempt frequency, the Boltzmann constant, the temperature, and the desorption energy barrier, with the value equaling the adsorption energy (E_a), respectively.

We use an attempt frequency of 10^{12} s^{-1} [45,46] and kT of 25.852 meV when T is 300 K. According to this formula, the larger the absolute value of the adsorption energy, the longer the recovery time. In this work, the recovery time of desorption of NH_3 from the substrate surface at 300 K is calculated, and the results are shown in Table 2. The predicted recovery times of NH_3 on the S-$HfSe_2$ surfaces with ε_x= 4%, 6% and 8% strained are 0.027 s, 1.153 s and 102.467 s, respectively, suggesting that NH_3 can be rapidly desorbed from the substrate surface. In addition, the results show that the recovery time of NH_3 from the O-$HfSe_2$ surface is longer, with the recovery time of 1.311×10^7 s at 300 K, as shown in Table 2. And after adsorption of NH_3, the band gap change rate of O-$HfSe_2$ is small (2.06%), indicating that its sensitivity to NH_3 is low, so O-$HfSe_2$ is not very suitable for detecting NH_3.

We have also added the comparison of adsorption energy (E_a), charge transfer (ΔQ), band gap change (ΔE_g) and band gap change rate ($\Delta E_g/E_g$) and recovery time (τ) for NH_3 gas adsorption by different materials, as shown in Table 2. It can be seen from the table that applying x-axis tensile strain to the S-$HfSe_2$ can increase the adsorption energy and charge transfer, and the charge transfer and change rate of band gap is larger than that of literature. The band gap change rate reaches the maximum at ε_x=4%, its corresponding recovery time is 0.027 s, indicating that the detection of NH_3 by S-$HfSe_2$ with ε_x=4% is sensitive and fast recovery.

4. Conclusion

In conclusion, pristine and X-doped $HfSe_2$ (X-$HfSe_2$, X=O, S, Te) monolayers have been used to study their interactions with NH_3 and O_3 according to first principles based on density function theory. The results show that the adsorption of NH_3 and O_3 by pristine $HfSe_2$ is weak. Their adsorption strength can be significantly improved by doping O. Chemisorption occurs between O-$HfSe_2$ and O_3 with largest charge transfer, and the band gap of O-$HfSe_2$ monolayer disappears after the

Table 2
Summary of adsorption energy (E_a), charge transfer (ΔQ), band gap change (ΔE_g) and band gap change rate ($\Delta E_g/E_g$) for NH_3 gas adsorption by different materials.

Substrate	E_a (eV)	ΔQ (e)	ΔE_g (eV)	$\Delta E_g/E_g$	τ (T = 300 K)	Reference
pure O—$HfSe_2$	−1.138	0.257	0.016	2.06%	1.311×10^7 s	This work
pure S-$HfSe_2$	−0.466	0.268	0.088	14.24%	67.368 μs	
2% S-$HfSe_2$	−0.501	0.274	0.107	16.31%	0.261 ms	
4% S-$HfSe_2$	−0.621	0.278	0.119	17.00%	0.027 s	
6% S-$HfSe_2$	−0.718	0.283	0.104	14.17%	1.153 s	
8% S-$HfSe_2$	−0.834	0.285	0.085	11.17%	102.467 s	
$PtAs_2$	−0.510	0.036	−0.010	−2.70%	0.370 ms	[47]
PtP_2	−0.500	0.033	−0.010	−3.57%	0.251 ms	
graphene	−0.316	−0.039	0.007	–	0.204μs	[48]
$MnPS_3$	−0.150	−0.010	0.008	0.36%	33.105 ns	[49]
WO_3(001)	−0.110	0.010	0.033	11.54%	704.561 ns	[50]

adsorption of O_3, indicating that O_3 has a great influence on its electrical properties, and further implies that O-$HfSe_2$ is not suitable as a O_3 gas sensor. Besides, the S-$HfSe_2$/NH_3 system has larger adsorption energy and charge transfer than O_3. However, it is still small. To enhance sensing performance of NH_3 by S-$HfSe_2$, the strain effect on the S-$HfSe_2$/NH_3 adsorption system is also studied. The results indicate that the adsorption strength of NH_3 on S-$HfSe_2$ can be enhanced by stretching S-$HfSe_2$ along x-axis. After absorbing NH_3, the conductivity of x-axis strained S-$HfSe_2$ changes obviously, which suggest its sensitivity. And the predicted recovery times of S-$HfSe_2$ surfaces with ε_x=4%, 6% and 8% 4 are 0.027 s, 1.153 s and 102.467 s, respectively, which indicates that x-axis strained S-$HfSe_2$ monolayer has potential applications prospect in NH_3 detecting. Furthermore, this study sheds light on gas-surface interactions, which may help in the future experimental development of two-dimensional materials for strain-based NH_3 sensing and performance optimization.

CRediT authorship contribution statement

Huiru Yang: Formal analysis, Investigation, Writing – original draft. **Junfeng Li:** Software, Investigation, Writing – review & editing. **Ziyuan Shao:** Methodology, Visualization. **Chunjian Tan:** Methodology, Investigation. **Chenshan Gao:** Data curation, Visualization. **Hongyuan Cui:** Investigation. **Xiaosheng Tang:** Visualization. **Yufei Liu:** Investigation. **Huaiyu Ye:** Supervision, Funding acquisition, Writing – review & editing, Validation. **Guoqi Zhang:** Funding acquisition.

Declaration of Competing Interest

The authors declare that they have no known competing financial interests or personal relationships that could have appeared to influence the work reported in this paper.

Acknowledgments

This work is supported by the National Key R&D Program of China (2018YFE0204600), the Shenzhen Fundamental Research Program (JCYJ20200109140822796), and the NSQKJJ under grant K21799119.

References

[1] J. Zhang, X. Liu, G. Neri, N. Pinna, Nanostructured materials for room-temperature gas sensors, Adv. Mater. 28 (2016) 795–831.
[2] X. Tang, A. Du, L. Kou, Gas sensing and capturing based on two-dimensional layered materials: overview from theoretical perspective, WIREs Comput. Mol. Sci. 8 (2018).
[3] H.T. Jung, The present and future of gas sensors, ACS Sens. 7 (2022) 912–913.
[4] S. Yang, C. Jiang, S.-h. Wei, Gas sensing in 2D materials, Appl. Phys. Rev. 4 (2017).
[5] D. Tyagi, H. Wang, W. Huang, L. Hu, Y. Tang, Z. Guo, Z. Ouyang, H. Zhang, Recent advances in two-dimensional-material-based sensing technology toward health and environmental monitoring applications, Nanoscale 12 (2020) 3535–3559.
[6] H.S. Tsai, Y. Wang, C. Liu, T. Wang, M. Huo, The elemental 2D materials beyond graphene potentially used as hazardous gas sensors for environmental protection, J. Hazard. Mater. 423 (2022), 127148.
[7] Q. Li, J. Meng, Z. Li, Recent progress on Schottky sensors based on two-dimensional transition metal dichalcogenides, J. Mater. Chem. A 10 (2022) 8107–8128.
[8] R. Kumar, N. Goel, M. Hojamberdiev, M. Kumar, Transition metal dichalcogenides-based flexible gas sensors, Sens. Actuators A 303 (2020).
[9] H. Li, Z. Yin, Q. He, H. Li, X. Huang, G. Lu, D.W. Fam, A.I. Tok, Q. Zhang, H. Zhang, Fabrication of single- and multilayer MoS2 film-based field-effect transistors for sensing NO at room temperature, Small 8 (2012) 63–67.
[10] R. Kumar, W. Zheng, X. Liu, J. Zhang, M. Kumar, MoS2-based nanomaterials for room-temperature gas sensors, Adv. Mater. Technol. 5 (2020).
[11] D. Zhang, M. Wang, W. Zhang, Q. Li, Flexible humidity sensing and portable applications based on MoSe2 nanoflowers/copper tungstate nanoparticles, Sens. Actuators B 304 (2020).
[12] S. Guo, D. Yang, S. Zhang, Q. Dong, B. Li, N. Tran, Z. Li, Y. Xiong, M.E. Zaghloul, Development of a cloud-based epidermal MoSe2 device for hazardous gas sensing, Adv. Funct. Mater. 29 (2019).
[13] H. Guo, C. Lan, Z. Zhou, P. Sun, D. Wei, C. Li, Transparent, flexible, and stretchable WS2 based humidity sensors for electronic skin, Nanoscale 9 (2017) 6246–6253.
[14] K.Y. Ko, J.G. Song, Y. Kim, T. Choi, S. Shin, C.W. Lee, K. Lee, J. Koo, H. Lee, J. Kim, T. Lee, J. Park, H. Kim, Improvement of gas-sensing performance of large-area tungsten disulfide nanosheets by surface functionalization, ACS Nano 10 (2016) 9287–9296.
[15] A. Eftekhari, Tungsten dichalcogenides (WS2, WSe2, and WTe2): materials chemistry and applications, J. Mater. Chem. A 5 (2017) 18299–18325.
[16] D.-.H. Baek, J. Kim, MoS2 gas sensor functionalized by Pd for the detection of hydrogen, Sens. Actuators B 250 (2017) 686–691.
[17] K.Y. Ko, S. Lee, K. Park, Y. Kim, W.J. Woo, D. Kim, J.G. Song, J. Park, J.H. Kim, Z. Lee, H. Kim, High-performance gas sensor using a large-area WS2 xSe2-2 x alloy for low-power operation wearable applications, ACS Appl. Mater. Interfaces 10 (2018) 34163–34171.
[18] S. Lebègue, T. Björkman, M. Klintenberg, R.M. Nieminen, O. Eriksson, Two-dimensional materials from data filtering and ab initio calculations, Phys. Rev. X 3 (2013).
[19] C. Gong, H. Zhang, W. Wang, L. Colombo, R.M. Wallace, K. Cho, Band alignment of two-dimensional transition metal dichalcogenides: application in tunnel field effect transistors, Appl. Phys. Lett. 103 (2013).
[20] R.Y. Yue, A.T. Barton, H. Zhu, A. Azcatl, L.F. Pena, J. Wang, X. Peng, N. Lu, L. X. Cheng, R. Addou, S. McDonnell, L. Colombo, J.W.P. Hsu, J. Kim, M.J. Kim, R. M. Wallace, C.L. Hinkle, HfSe2 thin films: 2D transition metal dichalcogenides grown by molecular beam epitaxy, ACS Nano 9 (2015) 474–480.
[21] Y.M. Jahn, A. Ya'akobovitz, Outstanding stretchability and thickness-dependent mechanical properties of 2D HfS2, HfSe2, and hafnium oxide, Nanoscale 13 (2021) 18458–18466.
[22] H. Cui, P. Jia, X. Peng, Adsorption of SO2 and NO2 molecule on intrinsic and Pd-doped HfSe2 monolayer: a first-principles study, Appl. Surf. Sci. 513 (2020).
[23] H. Cui, H. Zhu, P. Jia, Adsorption and sensing of SO2 and SOF2 molecule by Pt-doped HfSe2 monolayer: a first-principles study, Appl. Surf. Sci. 530 (2020).
[24] Z. Yan, M. Ji, J. Xia, H. Zhu, Recent advanced materials for electrochemical and photoelectrochemical synthesis of ammonia from dinitrogen: one step closer to a sustainable energy future, Adv. Energy Mater. 10 (2019).
[25] S. Giddey, S.P.S. Badwal, C. Munnings, M. Dolan, Ammonia as a renewable energy transportation media, ACS Sustain Chem Eng 5 (2017) 10231–10239.
[26] B. Timmer, W. Olthuis, A.v.d. Berg, Ammonia sensors and their applications—a review, Sens. Actuators B 107 (2005) 666–677.
[27] H.Y. Li, C.S. Lee, D.H. Kim, J.H. Lee, Flexible room-temperature NH3 sensor for ultrasensitive, selective, and humidity-independent gas detection, ACS Appl. Mater. Interfaces 10 (2018) 27858–27867.
[28] Z. Zhu, J.-.L. Chang, R.-.J. Wu, Fast ozone detection by using a core–shell Au@TiO2 sensor at room temperature, Sens. Actuators B 214 (2015) 56–62.
[29] Z. Zhu, J.-.L. Chang, C.-.H. Wu, T.-.L. Chou, R.-.J. Wu, Promotion effect of silver on Indium(III) oxide for detecting trace amounts of ozone, Sens. Actuators B 232 (2016) 442–447.
[30] Y.J. Onofre, A.C. Catto, S. Bernardini, T. Fiorido, K. Aguir, E. Longo, V. R. Mastelaro, L.F. da Silva, M.P.F. de Godoy, Highly selective ozone gas sensor based on nanocrystalline Zn0.95Co0.05O thin film obtained via spray pyrolysis technique, Appl. Surf. Sci. 478 (2019) 347–354.
[31] N. Sui, P. Zhang, T. Zhou, T. Zhang, Selective ppb-level ozone gas sensor based on hierarchical branch-like In2O3 nanostructure, Sens. Actuators B 336 (2021).

[32] B. Delley, DMol, a standard tool for density functional calculations: review and advances, Theor. Comput. Chem. 2 (1995) 221–254.
[33] J.H. Yuan, N.N. Yu, J.F. Wang, K.H. Xue, X.S. Miao, Design lateral heterostructure of monolayer ZrS2 and HfS2 from first principles calculations, Appl. Surf. Sci. 436 (2018) 919–926.
[34] S. Grimme, Semiempirical GGA-type density functional constructed with a long-range dispersion correction, J. Comput. Chem. 27 (2006) 1787–1799.
[35] J. Behler, Atom-centered symmetry functions for constructing high-dimensional neural network potentials, J. Chem. Phys. 134 (2011), 074106.
[36] C.S. Gao, Y.Y. Zhang, H.R. Yang, Y. Liu, Y.F. Liu, J.H. Du, H.Y. Ye, G.Q. Zhang, A DFT study of In doped Tl2O: a superior NO2 gas sensor with selective adsorption and distinct optical response, Appl. Surf. Sci. 494 (2019) 162–169.
[37] B. Delley, Hardness conserving semilocal pseudopotentials, Phys. Rev. B 66 (2002).
[38] B. Delley, An all-electron numerical method for solving the local density functional for polyatomic molecules, J. Chem. Phys. 92 (1990) 508–517.
[39] A. Abbasi, J.J. Sardroodi, Adsorption and dissociation of H2S on nitrogen-doped TiO2 anatase nanoparticles: insights from DFT computations, Surf. Interfaces 8 (2017) 15–27.
[40] H.-.Y. Song, J.-.J. Sun, M. Li, Enhancement of monolayer HfSe2 thermoelectric performance by strain engineering: a DFT calculation, Chem. Phys. Lett. (2021) 784.
[41] D.-.Y. Cho, C.H. Min, J. Kim, S.J. Oh, M.G. Kim, Bond nature of oxygen-deficient HfO2/Si(100) film, Appl. Phys. Lett. 89 (2006).
[42] H. Ye, L. Liu, Y. Xu, L. Wang, X. Chen, K. Zhang, Y. Liu, S.W. Koh, G. Zhang, SnSe monolayer: a promising candidate of SO2 sensor with high adsorption quantity, Appl. Surf. Sci. 484 (2019) 33–38.
[43] L. Liu, Q. Yang, Z. Wang, H. Ye, X. Chen, X. Fan, G. Zhang, High Selective Gas Detection for small molecules based on Germanium selenide monolayer, Appl. Surf. Sci. 433 (2018) 575–581.
[44] F. Opoku, P.P. Govender, Adsorption behaviour of Si anchored on g-C3N4/graphene van der Waals heterostructure for selective sensing of toxic gases: insights from a first-principles study, Appl. Surf. Sci. (2020) 525.
[45] H. Cui, X. Zhang, G. Zhang, J. Tang, Pd-doped MoS2 monolayer: a promising candidate for DGA in transformer oil based on DFT method, Appl. Surf. Sci. 470 (2019) 1035–1042.
[46] H. Yang, Y. Liu, C. Gao, L. Meng, Y. Liu, X. Tang, H. Ye, Adsorption behavior of nucleobases on doped MoS2 monolayer: a DFT study, J. Phys. Chem. C 123 (2019) 30949–30957.
[47] V.B. Zala, R.S. Shukla, P.D. Bhuyan, S.K. Gupta, P.N. Gajjar, Highly selective and reversible 2D PtX2 (X = P, As) hazardous gas sensors: ab-initio study, Appl. Surf. Sci. 563 (2021).
[48] X.-.Y. Liang, N. Ding, S.-.P. Ng, C.-M.L. Wu, Adsorption of gas molecules on Ga-doped graphene and effect of applied electric field: a DFT study, Appl. Surf. Sci. 411 (2017) 11–17.
[49] M. Jiang, K. Xu, N. Liao, H. Zhou, DFT investigation on highly selective NO2 sensing properties of MnPS3, Appl. Surf. Sci. 543 (2021).
[50] X. Cheng, X. Jiang, K. Tao, Q. Su, Y. Wang, E. Xie, Microscopic nature of gas adsorption on WO3 surfaces: electron interaction and localization, J. Phys. Chem. Lett. 11 (2020) 9070–9078.